Testing star formation laws on spatially resolved regions in a $z \approx 4.3$ starburst galaxy

P. Sharda [iD],[1,2]⋆ E. da Cunha,[1]⋆ C. Federrath,[1] E. Wisnioski [iD],[1,2] E. M. Di Teodoro [iD],[1,2] K. Tadaki [iD],[3] M. S. Yun,[4] I. Aretxaga[5] and R. Kawabe[3,6,7]

[1]*Research School of Astronomy and Astrophysics, Australian National University, Canberra ACT 2611, Australia*
[2]*ARC Centre of Excellence for All Sky Astrophysics in 3 Dimensions (ASTRO 3D), Australia*
[3]*National Astronomical Observatory of Japan, 2-21-1 Osawa, Mitaka, Tokyo 181-8588, Japan*
[4]*Department of Astronomy, University of Massachusetts, Amherst, MA 01003, USA*
[5]*Instituto Nacional de Astrofísica, Optica y Electrónica (INAOE), Aptdo. Postal 51 y 216, 72000 Puebla, Mexico*
[6]*SOKENDAI, The Graduate University for Advanced Studies, 2-21-1 Osawa, Mitaka, Tokyo 181-0015, Japan*
[7]*Department of Astronomy, School of Science, University of Tokyo, Bunkyo, Tokyo 113-0033, Japan*

ABSTRACT

We probe the star formation properties of the gas in AzTEC-1 in the COSMOS field, one of the best resolved and brightest starburst galaxies at $z \approx 4.3$, forming stars at a rate $> 1000 \, M_\odot \, yr^{-1}$. Using recent ALMA observations, we study star formation in the galaxy nucleus and an off-centre star-forming clump and measure a median star formation rate (SFR) surface density of $\Sigma_{SFR}^{nucleus} = 270 \pm 54$ and $\Sigma_{SFR}^{sfclump} = 170 \pm 38 \, M_\odot \, yr^{-1} \, kpc^{-2}$, respectively. Following the analysis by Sharda et al. (2018), we estimate the molecular gas mass, freefall time, and turbulent Mach number in these regions to predict Σ_{SFR} from three star formation relations in the literature. The Kennicutt–Schmidt (Kennicutt 1998; KS) relation, which is based on the gas surface density, underestimates the Σ_{SFR} in these regions by a factor 2–3. The Σ_{SFR} we calculate from the single-freefall model of Krumholz et al. (2012; KDM) is consistent with the measured Σ_{SFR} in the nucleus and the star-forming clump within the uncertainties. The turbulence-regulated star formation relation by Salim et al. (2015; SFK) agrees slightly better with the observations than the KDM relation. Our analysis reveals that an interplay between turbulence and gravity can help sustain high SFRs in high-redshift starbursts. It can also be extended to other high- and low-redshift galaxies thanks to the high-angular resolution and sensitivity of ALMA observations.

Key words: Turbulence – Stars: formation – galaxies: high-redshift – galaxy: kinematics and dynamics – galaxies: starburst – Submillimetre: galaxies.

1 INTRODUCTION

Understanding the formation and evolution of stars in the Universe remains one of the most pertinent questions in astrophysics. Deep surveys have established that the epoch of maximum star formation corresponds to redshifts $1 < z < 3$ (Madau & Dickinson 2014). As more and more starburst galaxies are found at $z \gtrsim 4$ with star formation rates (SFRs) exceeding $1000 \, M_\odot \, yr^{-1}$ (e.g. Coppin et al. 2010; Knudsen et al. 2010; Béthermin et al. 2016; Pavesi et al. 2018), it may imply that there is a higher fraction of them than previously estimated (Bower et al. 2006; Coppin et al. 2009). These galaxies are likely the progenitors of massive early-type galaxies found at $z \sim 2$ (Daddi et al. 2005; Capak et al. 2008). Therefore,

it is necessary to study the characteristics of such systems to get a comprehensive view of star formation from the earliest to the current epochs.

Following the analysis presented in Sharda et al. 2018 (hereafter, S18), we study the SFR in different regions of AzTEC-1, a non-lensed starburst galaxy at $z \approx 4.3$ discovered in the Cosmic Evolution Survey (COSMOS) field (Scoville et al. 2007), with the AzTEC camera (Wilson et al. 2008) on the *James Clarke Maxwell Telescope* (Scott et al. 2008). A follow-up survey by the Large Millimeter Telescope found its spectroscopic redshift to be 4.3420 ± 0.0004 (Yun et al. 2015). With a total $\lambda_{obs} = 860 \, \mu m$ continuum flux of $\sim 17 \, mJy$ and dust luminosity exceeding $10^{13} \, L_\odot$ (Tadaki et al. 2018; hereafter, T18), AzTEC-1 falls in the commonly used definition of submillimetre galaxies (SMGs, Hayward et al. 2011). S18 presented the first tests of different star formation relations on the spatially resolved star-forming nucleus of a high-

⋆ E-mail: piyush.sharda@anu.edu.au (PS); elisabete.dacunha@anu.edu.au (EDC)

redshift starburst galaxy. However, the necessity of excellent spatial resolution limited the analysis to the lensed source SDP 81. Now, with the ~550 pc resolution data at $z \approx 4.3$ from the Atacama Large Millimeter or Submillimeter Array (ALMA), we can test these relations at an even higher redshift in an unlensed clumpy disc galaxy. Such an analysis can help us understand what factors power high SFRs in high-redshift starbursts.

Section 2 summarizes the ALMA observations of the continuum emission (Iono et al. 2016; T18) and CO (4–3) transition (T18) of AzTEC-1 that we use in our work. Section 3 describes the calculation of the parameters that go into the star formation relations that we are testing. Section 4 discusses the comparison of the SFR we observe in AzTEC-1 with that predicted from various star formation relations published in the literature. Finally, we summarize our findings in Section 5. We adopt the ΛCDM cosmology with $H_0 = 70 \, \mathrm{km \, s^{-1} \, Mpc^{-1}}$, $\Omega_m = 0.27$, $\Omega_\Lambda = 1 \, \Omega_m$ (Spergel et al. 2003) and the Chabrier IMF (Chabrier 2003). The luminosity distance and scalelength corresponding to these parameters is 39.5 Gpc and 6.71 kpc $arcsec^{-1}$, respectively, for $z = 4.342$ (Wright 2006).

2 OBSERVATIONS

ALMA observations of the $\lambda_{obs} = 860 \, \mu m$ (Band 7) continuum emission in AzTEC-1 (centred at RA $= 09^h59^m42.85^s$, Dec. $= +02°29'38.23''$) were carried out in 2015 November (Iono et al. 2016). The $\lambda_{obs} = 3.2 \, mm$ (Band 3) continuum flux and CO (4–3) data were procured between 2017 October and November (T18). The observations and data reduction are described in detail in the respective articles. The angular resolution of the data is 0.093 × 0.072 arcsec, corresponding to 624 × 483 pc at $z \approx 4.3$ (T18). The total 860 μm, 3.2 mm fluxes, and the CO (4–3) velocity integrated flux measured by T18 are $S_{\nu,860}^{tot} \mu m = 17 \pm 1 \, mJy$, $S_{\nu,3.2\,mm}^{tot} = 273 \pm 41 \, \mu Jy$, and $S_{CO}^{tot} \, dv = 1.8 \pm 0.2 \, Jy \, km \, s^{-1}$, respectively.

Fig. 1 shows the $\lambda_{obs} = 860 \, \mu m$ continuum map and the CO (4–3) velocity structure of the galaxy. The continuum map shows the compact structure of the nucleus of the galaxy, with a few outlying clumps. The velocity map clearly shows a large-scale gradient in the galaxy probably owing to its rotational motion, as has been observed for numerous other high-redshift sources (e.g. Swinbank et al. 2015; Tadaki et al. 2017; Smit et al. 2018; Talia et al. 2018). We model the starburst nucleus as a Gaussian and define its diameter to be the full width at half-maximum (FWHM) of the resulting Gaussian fit of the 860 μm continuum map.[1] While the galaxy exhibits multiclump morphology, we find that a Gaussian fit local to the regions of interest (where the emission is peaked in the centre) is a good approximation for the flux distribution. The radius we obtain for the nucleus is $R = 0.46 \pm 0.05$ kpc. We also study one off-centre star-forming (SF) clump at RA $= 09^h59^m42.84^s$, Dec. $= +02°29'38.18''$. Like the nucleus, we also model this clump as a Gaussian and the FWHM gives us a radius of 0.24 ± 0.02 kpc. The following analyses are restricted to the nucleus and the SF clump because they are spatially distinct, have sufficient resolution to conduct the kinematic analysis (as we discuss in Section 3.2) and can be approximated to first order as spherical regions, to estimate their volume densities. Such an analysis can also inform us about the spatially diverse star formation history of the galaxy.

---

[1]We also use the CO (4–3) velocity integrated flux map to perform the fit and find an agreement with the 860 μm continuum map for the sizes of the nucleus and the SF clump to within 14 per cent and 21 per cent, respectively.
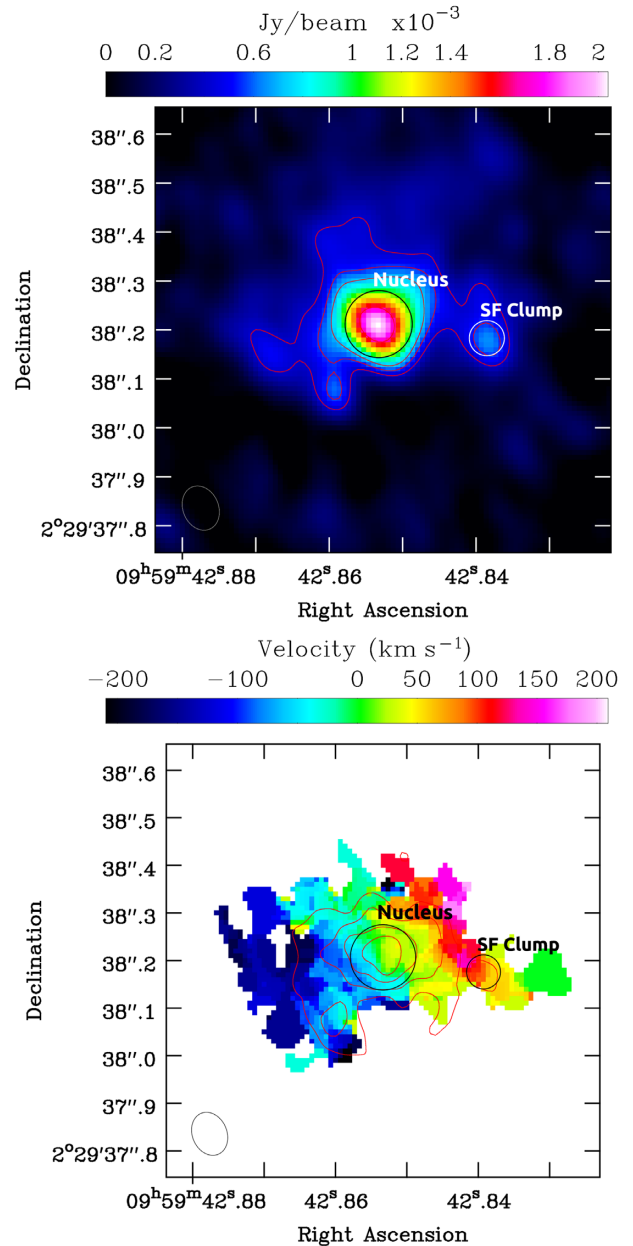
**Figure 1.** 0.093 × 0.072 arcsec (624 × 483 pc) resolution maps of $\lambda_{obs} = 860 \, \mu m$ continuum flux density and CO(4–3) velocity in AzTEC-1 (beam size as depicted in the lower left corners). The white and black circles in the two panels depict the nucleus and the SF clump we analyse in this work. The red contours in the continuum map correspond to 5, 7 and $9 \, \sigma_{860 \, \micron}$, while those on the velocity map correspond to CO(4–3) velocity integrated flux density, plotted at 5, 7, 9, and 11 $\sigma_{CO(4-3)}$.

3 PHYSICAL PARAMETERS FOR THE NUCLEUS AND SF CLUMP

In this Section, we measure the parameters that go into the three star formation relations we test in Section 4. We use a Monte Carlo analysis to estimate and propagate the uncertainties on all the parameters. We summarize the analysis in subsequent sub-sections, present the calculated quantities in Table 1, and refer the reader to S18 for details on the procedure.

Table 1. Properties of the two regions we study (nucleus and SF clump) in AzTEC-1 with the mean and the standard deviation quoted in brackets. For the SFR surface densities (Σ_{SFR}), we tabulate the median (standard deviation quoted in brackets) of their PDFs. We also report the difference between the median and the 16 and 84 percentiles of the different parameters (as subscripts and superscripts, respectively).

Parameter	Symbol / Unit	Nucleus	SF clump
Radius	R/kpc	0.46 (0.05)	0.24 (0.02)
Area	A/kpc^2	0.65 (0.13)	0.18 (0.04)
860 μm flux	$S_{\nu,860\,\mu m}$ mJy^{-1}	2.82 (0.11)	0.48 (0.02)
3.2 mm flux	$S_{\nu,3.2\,mm}$ μJy^{-1}	59 (7)	14 (4)
CO (4-3) flux	$S_{\nu,CO(4-3)}dv$/Jy km s^{-1}	0.24 (0.02)	0.052 (0.004)
Velocity dispersion	$\sigma_{v,turb}$/km s^{-1}	12 (1)	17 (2)
Mach number	$\mathcal{M}$	35 (16)	50 (20)
Gas mass	M_{gas}/10^9 M$_\odot$	9.9 (2.7)$^{+2.8}_{-0.9}$	1.9 (0.5)$^{+0.9}_{-0.4}$
Gas surface density	Σ_{gas}/10^{10} M$_\odot$ kpc^{-2}	1.5 (0.3)$^{+1.7}_{-0.5}$	1.0 (0.2)$^{+0.8}_{-0.3}$
Gas volume density	ρ/10^{-21} g cm^{-3}	1.8 (0.8)$^{+1.3}_{-0.5}$	2.4 (1.0)$^{+1.7}_{-0.6}$
Freefall time	t_{ff}/Myr	1.7 (0.5)$^{+0.9}_{-0.4}$	1.5 (0.3)$^{+0.8}_{-0.4}$
Measured SFR	Σ_{SFR}/M$_\odot$ yr^{-1} kpc^{-2}	270 (54)$^{+74}_{-105}$	170 (38)$^{+26}_{-39}$
Predicted SFRs	$\Sigma_{SFR,KS}$/M$_\odot$ yr^{-1} kpc^{-2}	105 (42)$^{+170}_{-75}$	62 (26)$^{+100}_{-20}$
	$\Sigma_{SFR,KDM}$/M$_\odot$ yr^{-1} kpc^{-2}	134 (47)$^{+240}_{-55}$	106 (40)$^{+190}_{-65}$
	$\Sigma_{SFR,SFK}$/M$_\odot$ yr^{-1} kpc^{-2}	270 (145)$^{+520}_{-120}$	280 (147)$^{+500}_{-115}$
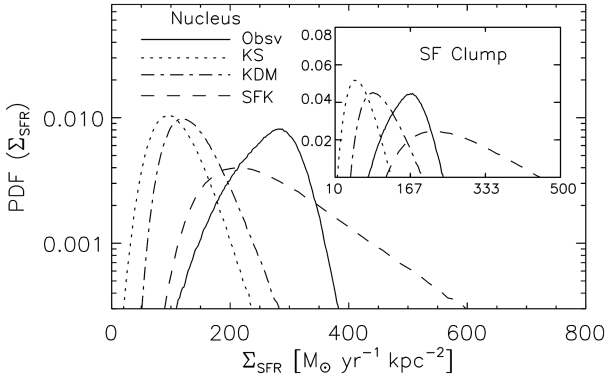
Figure 2. PDF of the SFR surface density (Σ_{SFR}) in the nucleus, estimated from the data and those predicted from KS (dotted curve, equation 1), KDM (dot–dashed curve, equation 2), and SFK (dashed curve, equation 3) relations. Inset depicts the same PDFs for the star-forming (SF) clump.

3.1 Star formation rate

We follow T18 to estimate the SFR per unit area in the two regions as $\Sigma_{SFR} = SFR^{tot} \times (S_{\nu,860\,\mu m}/S_{\nu,860\,\mu m}^{tot})/A$, where A is the effective area of the region that we find from the 2D Gaussian fit in Section 2, and SFR^{tot} is the total SFR of the galaxy. By fitting the spectral energy distribution (SED) of the galaxy at multiple wavelengths, T18 find $SFR^{tot} = 1186^{+36}_{-291}$ M$_\odot$ yr^{-1}.

We integrate the area under the modelled Gaussian curve to estimate the 860 μm flux in the two regions. For the nucleus and the SF clump, we obtain $S_{\nu,860\,\mu m} = 2.82 \pm 0.11$ mJy and 0.48 ± 0.02 mJy, respectively. We plot the probability density function (PDF) of the measured SFR surface densities (Σ_{SFR}) for the two regions in Fig. 2 (solid lines). The PDFs give the median SFR per unit area: $\Sigma_{SFR}^{nucleus} = 270 \pm 54$ M$_\odot$ yr^{-1} kpc^{-2} and $\Sigma_{SFR}^{sfclump} = 170 \pm 38$ M$_\odot$ yr^{-1} kpc^{-2} for the nucleus and the SF clump, respectively. SFR surface densities of similar magnitudes have been found in numerous other high-redshift starbursts (Hodge et al. 2015; Ikarashi et al. 2015; Enia et al. 2018; S18).

3.2 Velocity dispersion and mach number

As we see from Fig. 1, the CO (4–3) velocity map shows a large-scale velocity gradient in the galaxy due to its rotational motion. To extract the turbulent velocity features in the regions, we follow the analysis presented in section 4 of S18, *i.e.* we fit and subtract the local, linear velocity gradient in the regions (see also Federrath et al. 2016). This allows us to subtract the contributions of rotation to the dispersion and hence yields an estimate of the turbulent dispersion, provided there is enough spatial resolution. We use the resolution-check algorithm described in section 4.1 of S18 and find that we have sufficient resolution in the regions, which is necessary for the convergence of the derived turbulent velocity dispersion.

The turbulent velocity dispersion we obtain through the local, linear velocity gradient fit method in the nucleus and the SF clump are $\sigma_{v,turb} = 12 \pm 1$ km s^{-1} and 17 ± 2 km s^{-1}, respectively. We show the PDFs of the velocities in the regions before and after the subtraction of this gradient in Fig. 3. The gradient-subtracted velocity PDF is consistent with a Gaussian, like those estimated in other star-forming regions (Federrath et al. 2016; S18) and predicted by simulations of supersonic turbulence (Klessen 2000; Federrath 2013).

To independently check the validity of the local, linear gradient fit algorithm and given that the disc of AzTEC-1 is rotationally supported (T18), we also fit the CO data cube with a rotating disc model to account for the large-scale rotation of the galaxy and correct for beam smearing. For this purpose, we use the code ^{3d}BAROLO (Di Teodoro & Fraternali 2015) which fits tilted-ring models (Rogstad, Lockhart & Wright 1974) to spectroscopic data cubes and is applicable to multiwavelength observations (Salak et al. 2016; Sabatini et al. 2018). We present the model and the residual maps in Appendix A. The velocity dispersions we obtain for the nucleus and the SF clump are 13 and 23 km s^{-1}, respectively. From Fig. A1, we notice that the residual velocities in the nucleus do not show any residual gradient after subtraction (implying that the nucleus follows the galaxy-wide rotation) and is consistent with the velocity dispersion we obtain from the local, linear velocity gradient fit. However, we notice a leftover gradient in the SF clump
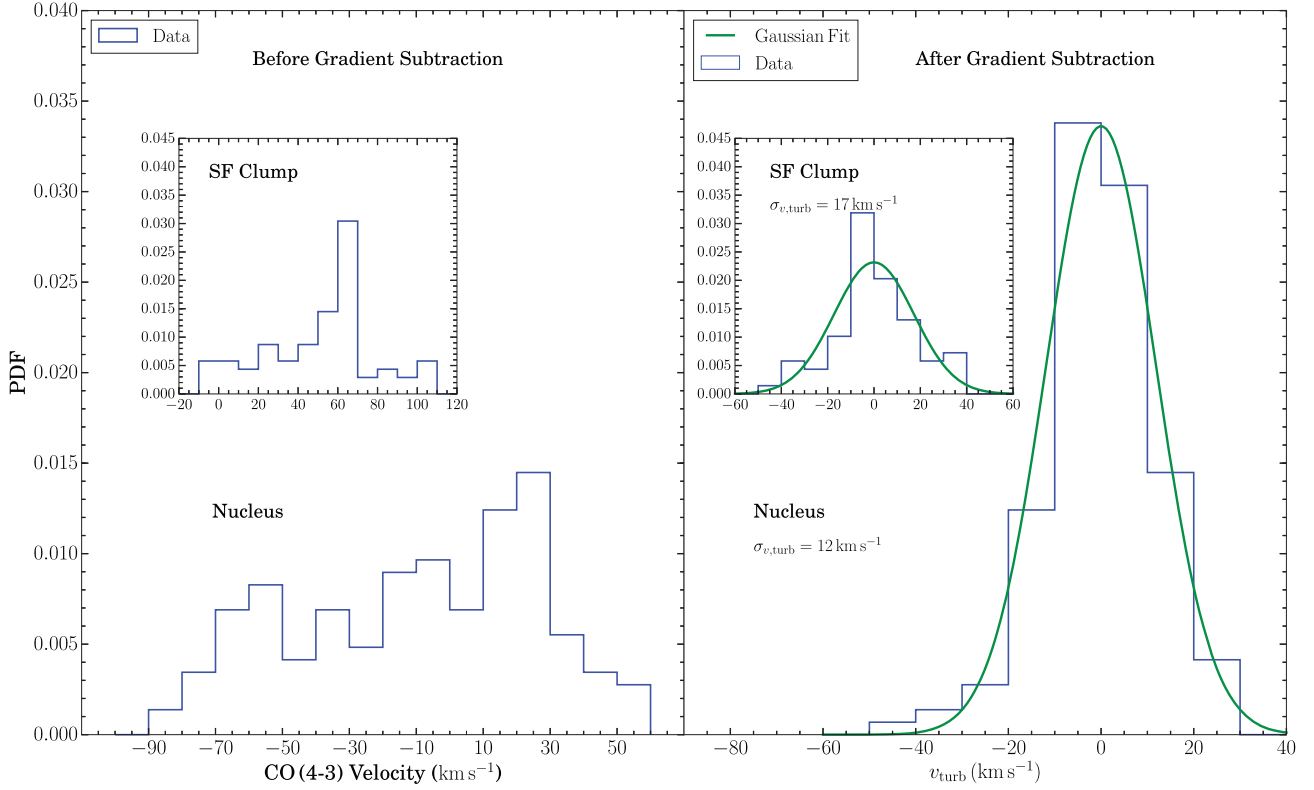
Figure 3. PDF of the CO (4–3) velocities (as labelled in Fig. 1) and velocities after the subtraction of the local, linear velocity gradient (v_{turb}). The standard deviation ($\sigma_{v,\text{turb}}$) of the turbulent velocity (gas velocity after gradient subtraction) yields the turbulent Mach number ($\mathcal{M}$) in the two regions. Inset depicts the same for the SF clump.

which, when accounted for using a local, linear gradient fit, gives a velocity dispersion of $18\,\text{km}\,\text{s}^{-1}$, in excellent agreement with what we obtain from the former method. This implies that the SF clump has some intrinsic rotation of its own which is different than the systematic galaxy-wide rotation which should be subtracted to reveal the turbulent features.

Assuming the temperature of the molecular gas in the two regions to be between 10 and 100 K, we find the sound speed as $c_s = 0.4 \pm 0.2\,\text{km}\,\text{s}^{-1}$ (e.g. Federrath et al. 2016), where the error represents the range of gas temperatures we consider. Then, the turbulent Mach number is given by: $\mathcal{M} = \sigma_{v,\text{turb}}/c_s$. The Mach numbers we obtain for the nucleus and the SF clump are 35 ± 16 and 50 ± 20, respectively. These Mach numbers are of the same order of magnitude as the few predicted for starburst environments at low and high redshifts (Salim, Federrath & Kewley 2015; Federrath et al. 2017, S18).

3.3 Molecular gas mass

CO is often used as a tracer for the cold and dense molecular gas present in star-forming regions because it is bright, easily observable due to its dipole moment and the second-most abundant molecule in star-forming regions (Daddi et al. 2015; Combes 2018). Following T18, we measure the molecular gas mass per unit area in the regions (Σ_{gas}) as: $\Sigma_{\text{gas}} = M_{\text{gas}}^{\text{tot}} \times (S_{\text{CO}}dv/S_{\text{CO}}^{\text{tot}}dv)/A$, where $S_{\text{CO}}^{\text{tot}}\,dv$ is the total CO (4-3) velocity-integrated flux density in the galaxy. The CO (4-3) velocity-integrated flux densities we find in the nucleus and the SF clump are $0.24 \pm 0.02\,\text{Jy}\,\text{km}\,\text{s}^{-1}$ and $0.052 \pm 0.004\,\text{Jy}\,\text{km}\,\text{s}^{-1}$ respectively. We convert them to CO (4-3)

line luminosities (Solomon & Vanden Bout 2005) and scale them to CO (1-0) line luminosities with the CO excitation scaling factor $r_{43} = L'_{\text{CO}(4-3)}/L'_{\text{CO}(1-0)}$. We follow T18 who set $r_{43} = 0.91$ to ensure consistency between CO and CI gas masses, however, we also experiment with $r_{43} = 0.46$, which is the average value for SMGs (Carilli & Walter 2013, see also Narayanan et al. 2011). This is a significant systematic that can change the derived SFRs by a factor of $\sim 2 - 3$ and we include it in our error propagation. We transform CO (1-0) line luminosity to gas (H$_2$) mass using a CO-to-H$_2$ conversion factor $\alpha_{\text{CO}} = 0.8 \pm 0.1\,\text{M}_\odot\,\text{K}^{-1}\,\text{km}^{-1}\,\text{s}\,\text{pc}^{-2}$ (Bolatto, Wolfire & Leroy 2013; Carilli & Walter 2013).

Putting these parameters together we find $M_{\text{gas}}^{\text{tot}} = (7.4 \pm 1.1) \times 10^{10}\,\text{M}_\odot$. The molecular gas masses we estimate for the two regions are $M_{\text{gas}} = (9.9 \pm 2.7) \times 10^9\,\text{M}_\odot$ and $(1.9 \pm 0.5) \times 10^9\,\text{M}_\odot$, respectively. We also estimate the gas masses from the dust masses that can be obtained from the Rayleigh–Jeans (RJ) tail of the SED (Magdis et al. 2012; Scoville et al. 2014, 2016), by assuming a gas-to-dust ratio of 100. The gas mass we get for the nucleus is $M_{\text{gas,RJ}} = (1.4 \pm 0.4) \times 10^{10}\,\text{M}_\odot$, in good agreement with that found using the CO (4-3) data. For the SF clump, we get $M_{\text{gas,RJ}} = (3.0 \pm 0.9) \times 10^9\,\text{M}_\odot$ which is consistent with the CO based gas mass within the systematic uncertainty.

Further, we calculate the gas surface density for the two regions as $\Sigma_{\text{gas}} = (1.5 \pm 0.3) \times 10^{10}\,\text{M}_\odot\,\text{kpc}^{-2}$ and $(1.0 \pm 0.2) \times 10^{10}\,\text{M}_\odot\,\text{kpc}^{-2}$, respectively. It is interesting to note that Σ_{gas} of the nucleus of AzTEC-1 is almost twice that of the nuclear region of SDP 81, but the rate of collapse of the gas is similar (as we show in Section 4.2). Table 1 summarizes all measured and derived parameters for the nucleus and the SF clump.

4 SFR PREDICTED BY DIFFERENT STAR FORMATION RELATIONS

4.1 Kennicutt–Schmidt (KS) relation

Firstly, we test the Kennicutt–Schmidt (KS, Kennicutt 1998) relation, which connects Σ_{gas} of a star-forming region to its SFR surface density (Σ_{SFR}) via a power law

$$\Sigma_{SFR,KS} = (1.6 \pm 0.4) \times 10^{-4} \left(\frac{\Sigma_{gas}}{M_\odot \, pc^{-2}} \right)^N M_\odot \, yr^{-1} \, kpc^{-2}, \quad (1)$$

where $N = 1.40 \pm 0.15$ was empirically derived by fitting the gas surface density against the SFR surface density, and the constant has been corrected for the Chabrier IMF (Tacconi et al. 2008; Da Cunha et al. 2010). We show the PDF of the Σ_{SFR} predicted by the KS relation as dotted lines in Fig. 2. The median of the PDFs give $\Sigma_{SFR,KS}^{nucleus} = 105 \pm 42$ and $\Sigma_{SFR,KS}^{sfclump} = 62 \pm 26 \, M_\odot \, yr^{-1} \, kpc^{-2}$. The KS relation underestimates the Σ_{SFR} in both regions by a factor 2–3. However, when the systematic uncertainty on r_{43} is included, the KS relation can explain the measured Σ_{SFR} to within 3σ for the nucleus.

4.2 Krumholz–Dekel–McKee (KDM) relation

We move on to the single-freefall model given by Krumholz et al. (2012; KDM), which also takes into account the freefall time of the gas under collapse in its prediction of Σ_{SFR}

$$\Sigma_{SFR,KDM} = f_{H_2} \epsilon_{ff} \frac{\Sigma_{gas}}{t_{ff}} , \quad (2)$$

where f_{H_2} is a factor of order unity and ϵ_{ff} is the star formation efficiency found to be 0.015 (Krumholz et al. 2013). t_{ff} is the freefall time-scale of collapse given by $t_{ff} = \sqrt{3\pi/32G\rho}$, where ρ is the volume density of the region. Following KDM, we approximate the two regions as regular spheres, and find the volume densities in the nucleus and the SF clump to be $\rho = (1.8 \pm 0.8) \times 10^{-21} \, g \, cm^{-3}$ and $(2.4 \pm 1.0) \times 10^{-21} \, g \, cm^{-3}$, respectively. Using these, the freefall time we obtain is $t_{ff} = 1.7 \pm 0.5 \, Myr$ and $1.5 \pm 0.3 \, Myr$, respectively. The median SFR surface densities we obtain from the KDM relation are $\Sigma_{SFR,KDM}^{nucleus} = 134 \pm 47$ and $\Sigma_{SFR,KDM}^{sfclump} = 106 \pm 40 \, M_\odot \, yr^{-1} \, kpc^{-2}$. We plot their PDFs in Fig. 2 (dash–dotted lines). Although the KDM relation underestimates the median Σ_{SFR} in the nucleus and the SF clump by a factor ~ 2 and 1.6 respectively, its predictions are consistent with the measured values when the systematic uncertainties are included. Further refinement may be possible as we move towards a larger sample.

4.3 Salim–Federrath–Kewley (SFK) relation

Salim et al. 2015 (SFK) extended the KDM relation to include the effects of physical variations of turbulence and magnetic field strength on star formation. Their multi-freefall model takes the form:

$$\Sigma_{SFR,SFK} = \epsilon_{ff} \frac{\Sigma_{gas}}{t_{ff}} \left[1 + b^2 \mathcal{M}^2 \frac{\beta_{mag}}{\beta_{mag} + 1} \right]^{3/8} , \quad (3)$$

where $\epsilon_{ff} = 0.0045$, b is the turbulent driving parameter (set to 0.4 to reflect a mixed turbulent driving mode, see Federrath et al. 2010; Federrath & Klessen 2012) and β_{mag} is the ratio of the thermal to magnetic pressure (Molina et al. 2012). We lack the magnetic field strength measurements for AzTEC-1; following S18, we set $\beta_{mag} \to \infty$ such that $\beta_{mag}/(\beta_{mag} + 1) = 1$. This means we assume that the magnetic field is zero.

The median of the PDF of Σ_{SFR} from the multifreefall SFK model is $\Sigma_{SFR,SFK}^{nucleus} = 270 \pm 145$ and $\Sigma_{SFR,SFK}^{sfclump} = 280 \pm 147 \, M_\odot \, yr^{-1} \, kpc^{-2}$. Fig. 2 (dashed lines) shows that the Σ_{SFR} we obtain from the SFK relation agrees with the measured Σ_{SFR} within the uncertainties. The slight overestimation of the Σ_{SFR} in the SF clump may be the result of ignoring magnetic fields in our calculations. It has been shown that finite, typical magnetic field strengths (for Milky Way conditions) can reduce SFRs by up to a factor of 2–3 (Padoan & Nordlund 2011; Federrath & Klessen 2012; Federrath 2015).

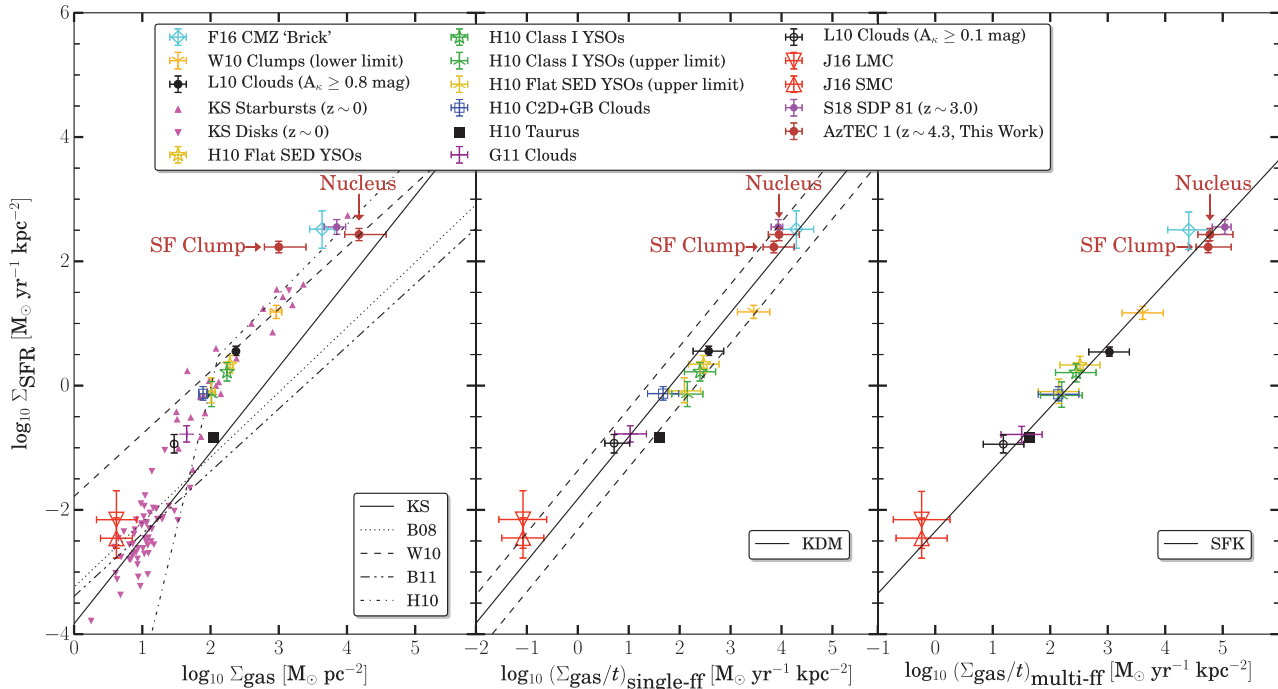## 4.4 Comparison of star formation relations across multiple data sets

We compare the measured SFRs in local star-forming regions with the high-redshift starburst galaxy SDP 81 ($z \approx 3.0$; S18) and AzTEC-1 ($z \approx 4.3$) against the three star formation relations we discussed. We present the comparison in Fig. 4, which has been adapted from S18. We also incorporate some other star formation relations based on gas surface densities in the left-hand panel of Fig. 4. These star formation relations do not predict reasonable SFRs for a large sub-set of the diverse sample.

When the freefall time of the gas is included (the KDM relation), some of the scatter in the measured SFR can be accounted for, as we show in the middle panel of Fig. 4. The remaining scatter is substantially lower in the SFK relation (right-hand panel of Fig. 4) compared to the KS and KDM relations. This is because the SFK relation does not only take gravity into account (as KDM does), but it also adds the physical effects of turbulence and magnetic fields, which are crucial for star formation (Krumholz & McKee 2005; Hennebelle & Chabrier 2011; Padoan & Nordlund 2011; Federrath & Klessen 2012; Federrath 2015). However, while the SFK relation has the physics of magnetic fields included, we cannot make use of that feature because we do not know the magnetic field strengths in high-redshift galaxies. Nevertheless, we find that the SFK relation best predicts the SFRs for both low- and high-redshift regions. Given the large systematic uncertainties that go in calculating the key ingredients, we require a large sample of diverse star-forming regions on multiple scales to fully assess the universality of these relations.

5 CONCLUSIONS

In this work, we probe the star formation characteristics of the starburst galaxy AzTEC-1 at redshift $z \approx 4.3$ in the COSMOS field. AzTEC-1 is one of the best resolved non-lensed galaxies at $z > 4$, and is interestingly forming stars at a rate $> 1000 \, M_\odot \, yr^{-1}$. It has a suitable environment to study the characteristics of star formation and understand how high-redshift ($z > 4$) galaxies can sustain such high SFRs. Following the methodology described in Sharda et al. (2018), we use spatially resolved (sub-kiloparsec scale) ALMA observations of the sub-millimetre continuum and CO (4–3) emission to test the validity of three star formation relations in the literature. In particular, we study the galaxy nucleus and an off-centre star-forming (SF) clump in this galaxy because they have sufficient resolution to apply the kinematic analysis.

The nucleus of AzTEC-1 has a very compact structure, with a gas surface density (Σ_{gas}) 2 times the nucleus of the starburst galaxy SDP 81 at $z \approx 3.0$. However, its median SFR surface density (Σ_{SFR}) is only 70 per cent of the latter, possibly because it is one-third as turbulent. Similarly, while the Σ_{gas} of the SF clump in AzTEC-1 is almost an order of magnitude lower than the galaxy nucleus

Figure 4. Comparison of star formation relations in multiple data sets, showing the measured and predicted SFRs, overlaid with the two regions of AzTEC-1 in brown. Asymmetric error bars for AzTEC-1 regions are a result of the systematic uncertainty on the CO excitation scale factor r_{43}. *Left-hand panel:* Measured SFR surface density as a function of the gas surface density (equation 1) in numerous star-forming regions (Heiderman et al. (2010); H10), Lada, Lombardi & Alves 2010; L10), Wu et al. (2010; W10), Gutermuth et al. (2011; G11), Jameson et al. (2016; J16), Federrath et al. (2016; F16) and Sharda et al. (2018; S18)). Also plotted are the SFR relations proposed by Bigiel et al. (2008; B08), Bigiel et al. (2011; B11), Wu et al. (2010; W10), and Heiderman et al. (2010; H10). *Middle-panel:* Measured SFR surface density plotted against the single-freefall time model by Krumholz, Dekel & McKee (2012; equation 2). The dashed lines depict deviations by a factor of 3 from the best-fitting relation (see also Krumholz, Dekel & McKee 2013). *Right-hand panel:* Measured SFR surface density plotted against the multi-freefall model of Salim et al. (2015; equation 3).

in AzTEC-1, the Σ_{SFR} of the former is only two-fifth as high as the latter, possibly because it is 1.4 times more turbulent. While turbulence acts against star formation by stabilizing the cloud to prevent collapse on large scales, supersonic turbulence can create local shock-compressed regions which are the progenitors of star formation sites (Hennebelle & Chabrier 2011; Roman-Duval et al. 2011; Federrath & Klessen 2012). Thus, an interplay between gravity and turbulence seems to play a major role in sustaining high SFRs in these starbursts. We also find that the SF clump has an intrinsic rotation of its own, which does not follow the galaxy-wide rotation. Such a star-forming clump reflects the spatially diverse star formation history of the galaxy and adds valuable information about its past evolution.

We show that the Kennicutt–Schmidt (KS) relation underestimates the Σ_{SFR} in both the regions in AzTEC-1 by a factor of 2–3. The single-freefall model by Krumholz et al. (2012; KDM) underestimates the median Σ_{SFR} in the nucleus and the SF clump by a factor ~ 2 and 1.6, respectively; however, these predictions are within the systematic uncertainties. The multi-freefall model by Salim et al. (2015; SFK) gives median Σ_{SFR} consistent with that measured in the nucleus and overpredicts it for the SF clump by 60 per cent. The slight overestimation from the (SFK) relation possibly arises because we lack the magnetic field strength in the galaxy, and neglect its effect on Σ_{SFR}. AzTEC-1 thus forms a part of the very few star-forming galaxies (and the only galaxy at $z \gtrsim 2$, apart from SDP 81) for which the KDM and SFK relations have been tested.

Examining the performance of these relations across multiple data sets and given all the caveats, we conclude that the SFK

relation provides the best prediction for the SFR in low- and high-redshift star-forming regions. We also find that an interplay between turbulence and gravity can help sustain high SFRs in high-redshift starburst galaxies. Our method can be used to reproduce the same analysis for other local and high-redshift star-forming regions on spatially resolved scales, which can inform us about the diverse star formation history of these regions.

REFERENCES

Béthermin M. et al., 2016, A&A, 586, 5
Bigiel F. et al., 2011, ApJ, 730, 6
Bigiel F., Leroy A., Walter F., Brinks E., de Blok W. J. G., Madore B., Thornley M. D., 2008, AJ, 136, 2846
Bolatto A. D., Wolfire M., Leroy A. K., 2013, ARA&A, 51, 207
Bower R. G., Benson A. J., Malbon R., Helly J. C., Frenk C. S., Baugh C. M., Cole S., Lacey C. G., 2006, MNRAS, 370, 645
Capak P. et al., 2008, ApJ, 681, L53
Carilli C. L., Walter F., 2013, ARA&A, 51, 105
Chabrier G., 2003, ApJ, 586, L133
Combes F., 2018, A&A Rev., 26, 31
Coppin K. E. K. et al., 2009, MNRAS, 395, 1905
Coppin K. E. K. et al., 2010, MNRAS, 407, L103
da Cunha E., Eminian C., Charlot S., Blaizot J., 2010, MNRAS, 403, 1894
Daddi E. et al., 2005, ApJ, 626, 680
Daddi E. et al., 2015, A&A, 577, 19
Di Teodoro E. M., Fraternali F., 2015, MNRAS, 451, 3021
Enia A. et al., 2018, MNRAS, 475, 3467
Federrath C. et al., 2016, ApJ, 832, 18
Federrath C. et al., 2017, MNRAS, 468, 3965
Federrath C., 2013, MNRAS, 436, 1245
Federrath C., 2015, MNRAS, 450, 4035
Federrath C., Klessen R. S., 2012, ApJ, 761, 156
Federrath C., Roman-Duval J., Klessen R. S., Schmidt W., Mac Low M.-M., 2010, A&A, 512, 28
Gutermuth R. A., Pipher J. L., Megeath S. T., Myers P. C., Allen L. E., Allen T. S., 2011, ApJ, 739, 84
Hayward C. C., Kereš D., Jonsson P., Narayanan D., Cox T. J., Hernquist L., 2011, ApJ, 743, 159
Heiderman A., Evans N. J., II, Allen L. E., Huard T., Heyer M., 2010, ApJ, 723, 1019
Hennebelle P., Chabrier G., 2011, ApJ, 743, L29
Hodge J. A., Riechers D., Decarli R., Walter F., Carilli C. L., Daddi E., Dannerbauer H., 2015, ApJ, 798, L18
Ikarashi S. et al., 2015, ApJ, 810, 12
Iono D. et al., 2016, ApJ, 829, 6
Jameson K. E. et al., 2016, ApJ, 825, 24
Kennicutt R. C., Jr., 1998, ApJ, 498, 541
Klessen R. S., 2000, ApJ, 535, 869
Knudsen K. K., Kneib J.-P., Richard J., Petitpas G., Egami E., 2010, ApJ, 709, 210
Krumholz M. R., McKee C. F., 2005, ApJ, 630, 250
Krumholz M. R., Dekel A., McKee C. F., 2012, ApJ, 745, 69
Krumholz M. R., Dekel A., McKee C. F., 2013, ApJ, 779, 89
Lada C. J., Lombardi M., Alves J. F., 2010, ApJ, 724, 687
Madau P., Dickinson M., 2014, ARA&A, 52, 415
Magdis G. E. et al., 2012, ApJ, 760, 23
Molina F. Z., Glover S. C. O., Federrath C., Klessen R. S., 2012, MNRAS, 423, 2680
Narayanan D., Cox T. J., Hayward C. C., Hernquist L., 2011, MNRAS, 412, 287
Padoan P., Nordlund Å., 2011, ApJ, 730, 40
Pavesi R. et al., 2018, ApJ, 861, 16
Rogstad D. H., Lockhart I. A., Wright M. C. H., 1974, ApJ, 193, 309
Roman-Duval J., Federrath C., Brunt C., Heyer M., Jackson J., Klessen R. S., 2011, ApJ, 740, 120

Sabatini G., Gruppioni C., Massardi M., Giannetti A., Burkutean S., Cimatti A., Pozzi F., Talia M., 2018, MNRAS, 476, 5417
Salak D., Nakai N., Hatakeyama T., Miyamoto Y., 2016, ApJ, 823, 68
Salim D. M., Federrath C., Kewley L. J., 2015, ApJ, 806, L36
Scott K. S. et al., 2008, MNRAS, 385, 2225
Scoville N. et al., 2007, ApJS, 172, 38
Scoville N. et al., 2014, ApJ, 783, 13
Scoville N. et al., 2016, ApJ, 820, 21
Sharda P., Federrath C., da Cunha E., Swinbank A. M., Dye S., 2018, MNRAS, 477, 4380
Smit R. et al., 2018, Nature, 553, 178
Solomon P. M., Vanden Bout P. A., 2005, ARA&A, 43, 677
Spergel D. N. et al., 2003, ApJS, 148, 175
Swinbank A. M. et al., 2015, ApJ, 806, 5
Tacconi L. J. et al., 2008, ApJ, 680, 246
Tadaki K. et al., 2017, ApJ, 841, 6
Tadaki K. et al., 2018, Nature, 560, 613
Talia M. et al., 2018, MNRAS, 476, 3956
Wilson G. W. et al., 2008, MNRAS, 386, 807
Wright E. L., 2006, PASP, 118, 1711
Wu J., Evans N. J., II, Shirley Y. L., Knez C., 2010, ApJS, 188, 313
Yun M. S. et al., 2015, MNRAS, 454, 3485

APPENDIX A: KINEMATIC MODELLING

In this Appendix, we give details on the kinematic modelling of AzTEC-1 with the ^{3d}BAROLO software. ^{3d}BAROLO fits 3D tilted-ring models directly to emission-line data cubes, reducing the impact of the beam smearing effect on the derived kinematical parameters (see Di Teodoro & Fraternali 2015, for details). For the kinematic modelling, we use the ALMA data cube of the CO (4–3) emission line. We fix the geometry of the galaxy to the best-fitting parameters found by Tadaki et al. (2018): we assume a kinematic centre (RA$_c$, Dec$_c$) = $(09^h59^m42.85^s, +02°29'38.23'')$, an inclination angle of the galaxy disc with respect to the line-of-sight $i = 44°$, and a position angle of the receding part of the galaxy major axis $\phi = 296°$ (measured counterclockwise from the North direction). A mask is built by smoothing the ALMA CO data cube to a resolution of 0.2 arcsec and by running the source finding algorithm on the smoothed data cube with a signal to noise cut of 2.5. During the modelling procedure, we use a ring width of 0.04 arcsec, about half the FWHM of the beam, and we fit the rotation velocity and velocity dispersion only.

Fig. A1 shows our best-fitting model compared to the observations. Panels (a), (b), and (c) denote the data, model, and residual velocity fields, respectively. Panels (d) and (e) show position–velocity diagrams extracted along the major and minor axes, respectively. The data are in grey-scale and black contours, the model is represented with red thick contours. Overall, the model traces the data reasonably well. The high-velocity CO emission visible near the centre of the galaxy, which is not reproduced by our simple rotating model, may be due to the presence of strong non-circular motions and/or a starburst-driven outflow. Panel (f) is the rotation curve (inclination-corrected), panel (g) the velocity dispersion profile. We note that our rotation velocity of ∼220 km s^{-1} in the external regions is in good agreement with the maximum rotation velocity of 227 km s^{-1} quoted in Tadaki et al. (2018). However, we find an average intrinsic gas velocity dispersion of ∼50 km s^{-1}, a value slightly lower than the 74 km s^{-1} found by Tadaki et al. (2018). This discrepancy might be due to the different techniques used to fit the kinematics of the galaxy as well as to the uncertainties related to the large velocity channel width (∼30 km s^{-1}) of the ALMA data.
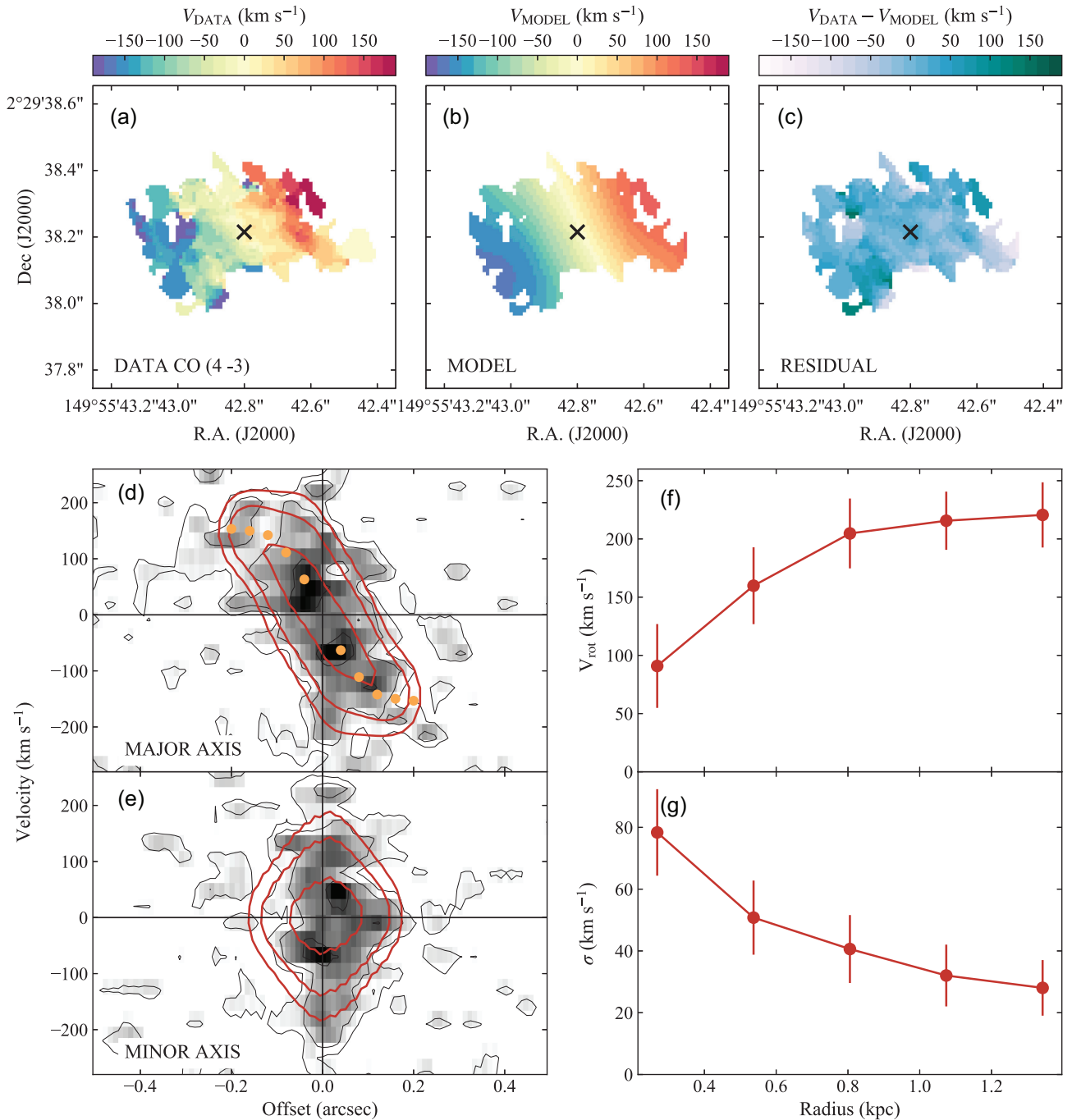
Figure A1. Kinematic modelling of AzTEC-1 with ³ᵈBAROLO. Panels (a)-(b)-(c): observed velocity field (same as Fig. 1), model velocity field, and residuals (data-model). Black crosses represent the kinematic centre of the galaxy. Panels (d)-(e): position-velocity cuts taken along the major and minor axes of the galaxy. Data are shown in grey-scale and black contours, model in red contours. Contour levels are at 1.5, 3, and $5\sigma_{\mathrm{RMS}}$, with $\sigma_{\mathrm{RMS}} = 78\,\mu\mathrm{Jy}$ being the rms noise of the data. Orange dots in panel (d) denote the derived rotation velocity (not corrected for inclination). Panels (f)-(g): rotation curve and velocity dispersion profile along the line of sight.

This paper has been typeset from a TₑX/LATₑX file prepared by the author.